Computational Materials Science 50 (2010) 211–217

Contents lists available at ScienceDirect

Computational Materials Science

journal homepage: www.elsevier.com/locate/commatsci

Effects of pores on shear bands in metallic glasses: A molecular dynamics study

Jiangting Wang[a], Peter D. Hodgson[a], Jingde Zhang[b], Wenyi Yan[c], Chunhui Yang[d,*]

[a] Centre for Material and Fibre Innovation, Deakin University, Waurn Ponds, VIC 3217, Australia
[b] Key Lab for Liquid Structure and Heredity of Materials of Ministry of Education, Shandong University, Jinan 250061, China
[c] Department of Mechanical and Aerospace Engineering, Monash University, Clayton, VIC 3800, Australia
[d] School of Engineering, Deakin University, Waurn Ponds, VIC 3217, Australia

ARTICLE INFO

Article history:
Received 18 May 2010
Received in revised form 16 July 2010
Accepted 2 August 2010
Available online 30 August 2010

Keywords:
Porous metallic glasses
Molecular dynamics
Shear bands
Deviatoric shear strains
Nanoindentation
Uniaxial compression

ABSTRACT

The effects of nanoscale pores on the strength and ductility of porous $Cu_{46}Zr_{54}$ metallic glasses during nanoindentation and uniaxial compression tests are modelled and investigated using molecular dynamics (MD) simulations. In the MD simulations, atomistic amorphous samples were digitally prepared through fast quenching from the liquid states of copper and zirconium alloy. In both of the nanoindentation and uniaxial compression simulations, shear transformation zones and shear bands are observed through the local deviatoric shear strains in the samples. The results show that the existence of pores causes strain concentrations and greatly promotes the initialization and propagation of shear bands. Importantly, only pores reaching critical size can effectively facilitate the formation of multiple shear bands. It is also observed that hardening occurs through pore annihilation and the shear band stops in porous metallic glasses.

1. Introduction

Newly-developed metallic glasses have combination of high yield strength and elastic limit, which for some time has suggested that they could form a new generation of structural engineering materials [1–3]. However, metallic glasses usually show no macroscopic plasticity, due to the localization of plastic flow in shear bands, which nucleate and propagate globally and lead to the failure [3–6]. This catastrophic failure mode significantly limits the applications of metallic glasses. Therefore, many researchers have studied the behaviours of such shear bands to improve the ductility [7–16].

Recently, porous metallic glasses with an average pore size ranging from 25 nm to 10 μm have been fabricated using a series of techniques [17–23]. In general, the roles of pores in metallic glasses are to introduce strain concentrations and act as initiation sites of shear bands, resulting in the formation of multiple shear bands and the dissipation of the plastic strain [20–22]. It has been shown that a high-porosity metallic glass exhibits stable plastic deformation, increasing the macroscopic compressive strain up to 80% without failure [17]. However, due to the lack of detailed experimental observations of shear band formation and propagation, several essential questions concerning about porous metallic glasses have not been answered. These include: (i) how the size of pores affects the initiation and propagation of shear bands, (ii) how pores evolve during the deformation of porous metallic glasses, and (iii) how pores contribute to the plasticity and toughness of these materials.

In the study, molecular dynamics (MD) simulations are employed to model the nanoindentation and unaxial compression of both bulk and porous $Cu_{46}Zr_{54}$ metallic glasses. Porous amorphous samples with pores of different size are numerically generated and tested to study their effects on the shear banding mechanism.

2. Molecular dynamics simulations

2.1. Potential function used in MD models

A many-body potential based on the tight-binding scheme [24,25] was adopted to describe the $Cu_{46}Zr_{54}$ metallic glass system. The tight-binding potential is composed of the interactive band energy and repulsive pairwise energy. For an individual atom, *i*, its energy can be expressed as,

$$E_i = \sum_{i \neq j} A_{\alpha\beta} \exp\left[-p_{\alpha\beta}\left(\frac{r_{ij}}{r_0^{\alpha\beta}} - 1\right)\right] - \left\{\sum_{i \neq j} \xi_{\alpha\beta}^2 \exp\left[-2q_{\alpha\beta}\left(\frac{r_{ij}}{r_0^{\alpha\beta}} - 1\right)\right]\right\}^{1/2} \tag{1}$$

where α and β denote atom types, r_{ij} is the distance between atom *i* and its neighbour atom *j*, $r_0^{\alpha,\beta}$ represents the first-neighbour distance

---

* Corresponding author. Tel.: +61 03 52272082; fax: +61 03 52272167.
E-mail address: chunhui.yang@deakin.edu.au (C. Yang).

0927-0256/$ - see front matter © 2010 Elsevier B.V. All rights reserved.
doi:10.1016/j.commatsci.2010.08.001

Table 1
Parameters for tight-binding potential of $Cu_{46}Zr_{54}$ system [26].

	r_0 (Å)	A (eV)	ξ (eV)	p	q
Cu–Cu	2.6356	0.1074	1.3483	10.2215	2.7490
Cu–Zr	2.9086	0.1808	2.0100	8.6020	2.7960
Zr–Zr	3.2100	0.1844	2.3365	7.9273	2.0250

of an $\alpha\beta$ atom pair, $\xi_{\alpha\beta}$ is an effective hopping integral, and $q_{\alpha\beta}$ describes its dependence on the relative interatomic distance. Both $q_{\alpha\beta}$ and $\xi_{\alpha\beta}$ are assumed to depend only on the interacting atomic species α and β, and $A_{\alpha\beta}$ and $p_{\alpha\beta}$ are parameters of pairwise energy. Table 1 shows the parameters of tight-binding potential for $Cu_{46}Zr_{54}$ metallic glasses system with a cutoff distance of 4.5 Å [26].

2.2. MD simulation setups

The initial atomistic configuration of the MD simulations was a B2 structured block with a size of $\sim 13 \times 13 \times 2.5\ \mathrm{nm}^3$ containing 21,600 Cu and Zr atoms in total, maintaining the composition of $Cu_{46}Zr_{54}$. With periodic boundary conditions applied, the B2 $Cu_{46}Zr_{54}$ block was heated to 2100 K and equilibrated for 0.5 ns, then quenched to 100 K at a cooling rate of 20 K/ns and equilibrated at 100 K for 0.5 ns to obtain a stable amorphous structure [27]. The temperature and the pressure were controlled with the Nose–Hoover thermostat and Nose–Hoover barostat [28–31]. All MD simulations were performed with a classical molecular dynamics code LAMMPS [32] and post-processed with Atomeye [33] for visualization.

In the simulations for the nanoindentation, the amorphous block was replicated 8 × 3 in x–y plane resulting in a slab with a size of $\sim 101 \times 38 \times 2.5\ \mathrm{nm}^3$, which was referred as bulk sample N-Bulk. This model was designed for a thin film on a substrate as shown in Fig. 1a. The x and y dimensions were relatively large compared to the z dimension to reproduce a plane-strain condition. Periodic boundary conditions were imposed in both x and z dimensions. The top face in y dimension was a free surface and the bottom face of 1 nm thick was fixed to simulate support from a substrate. A cylindrical indenter was applied to repel each atom that touches it, with a force of magnitude:

$$F(r) = -K(r - R)^2 \tag{2}$$

where K is the specified force constant, r is the distance from the atom to the axis of the indenter, and R is the radius of the indenter. Specifically, the radius of the cylindrical indenter was 40 nm, and the constant K was 100 in current model. Hence, this indenter was regarded as a high stiffness material with no surface friction. The nanoindentation simulations were performed in depth-controlled mode, in which the indenter was displaced at a rate of 2 m/s in the negative y direction until a maximum indentation depth of 4.8 nm was reached. Then, the indenter was hold at the maximum indentation depth for 0.5 ns before unloading. Throughout nanoindentation, the temperature was maintained at 100 K and the external pressure in z dimension was maintained at zero. Apart from the bulk sample, two cases of interacting between pores and nanoindentations were studied: (i) the indenter was applied right above a single pore in porous material, referred as sample N-A; and (ii) the indenter was applied along the midline of two pores in porous material, referred as sample N-B. All the pores were conveniently created by extruding circles of radius 1.5 nm in the x–y plane. In order to minimize the surface free energy, the porous samples were equilibrated at 100 K and zero pressure for 0.5 ns prior to loading the indenter. In fact, since periodic boundary conditions were applied in z dimension, the pores are actually hollow cylinders of infinite lengths.

For the simulation of uniaxial compression, the amorphous block was similarly replicated 3 × 6 in x–y plane to create a single slab with a size of $\sim 38 \times 76 \times 2.5\ \mathrm{nm}^3$, referred as bulk sample C-Bulk. The schematic of the uniaxial compression simulations is depicted in Fig. 1b. Uniaxial compressions were achieved by displacing the boundaries of y dimension at a constant engineering strain rate of $0.1\ \mathrm{ns}^{-1}$, up to a maximum displacement corresponding to 30% engineering strain. The equivalent displacement rate was about 7.6 m/s, which was relatively high, compared to that of experimental compression tests, but it was still far below the sound speed of metallic glass samples ($\sim 1.0 \times 10^3$ m/s). Similarly, periodic boundary conditions were imposed along the y and z dimensions, while free surfaces were employed in x dimension. The temperature was maintained at constant 100 K and the external pressure in z dimension was maintained at zero throughout the uniaxial compressions. Three porous samples were numerically prepared by extruding circles on the x–y plane with an identical radius of 1.5 nm, 2.0 nm, and 2.5 nm, which were referred as porous samples C-PI, C-PII, and C-PIII, respectively. The 10 pores are uniformly distributed over each samples, with each pore has the same distance to neighbouring pores or boundary. Before uniaxial compression, the porous samples were also equilibrated at 100 K and zero pressure for 0.5 ns. The resulting porosity was 2.4% for porous sample C-PI, 4.3% for porous sample C-PII, and 6.8% for porous sample C-PIII.

2.3. Characterization of shear strains

The shear transformation zones and shear bands were visualized with the local deviatoric shear strains [34]. Since strains are

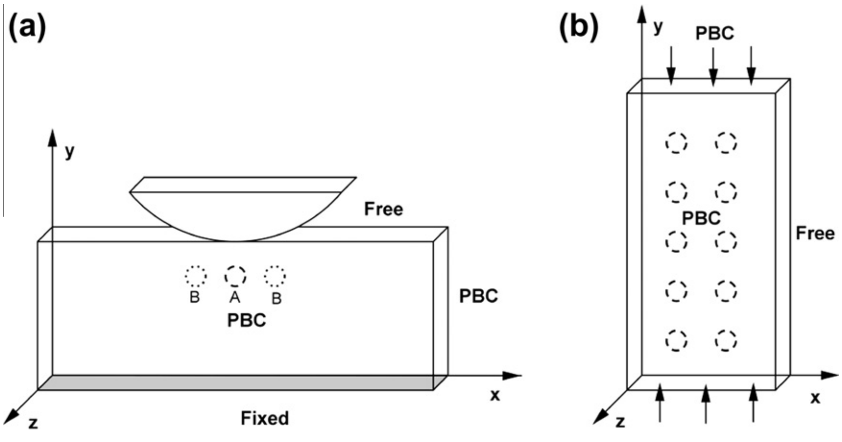

Fig. 1. Schematics of MD models for: (a) nanoindentation and (b) unaxial-compression.

a relative measurement, two states are needed in order to calculate it, the current state $r(t)$ and the reference state $r(t-\Delta t)$. When an atomistic configuration deforms from its reference configuration, atoms move into new positions, resulting in the change in neighbourhood of atoms. For each atom, the displacements of its neighbour atoms can be calculated by comparing the current and reference configurations. A variable that represents the degree of deformation is defined as the sum of squared deviation between the actual displacements of the neighbouring atoms and the virtual displacements that were compatible with a region having a uniform strain ε_{ij} [34], expressed as,

$$D^2(t,\Delta t) = \sum_n \sum_i \left\{ r_n^i(t) - r_0^i(t) - \sum_j (\delta_{ij}+\varepsilon_{ij}) \times \left[r_n^j(t-\Delta t) - r_0^j(t-\Delta t) \right] \right\}^2 \qquad (3)$$

where the indices i and j denote spatial coordinates and the index n runs over the neighbour atoms within the cutoff distance. The cutoff distance used in this calculation usually needs to be larger than the cutoff distance in potential function, because the local deformation field can extend to several atom radii, i.e. a cutoff distance of 8.0 Å is used in current calculation of D^2 $(t, \Delta t)$. Then, the local deviatoric shear strains, ε_{ij}, were determined by minimizing the value of D^2 $(t, \Delta t)$ through a least square fitting.

The local deviatoric shear strains characterize the incremental deformation between two selected states, namely, current and reference configuration. Hence, the calculated local deviatoric shear strains are depending on the selection of the reference configuration. If both of the current and reference configuration are in the proceeding of deformation, then the calculated local deviatoric shear strains are termed as the incremental deviatoric shear strains. If the initial state before deformation is chosen as the reference configuration, the local deviatoric shear strains characterize the total deformation that has occurred up to the current state, which are termed as the net deviatoric shear strains. In the following sections, the local deviatoric shear strains are the net deviatoric shear strains, as the initial states are always chosen as the reference configuration.

3. Results and discussion

3.1. Evolution of shear bands under nanoindentation loading conditions

In the MD simulations of nanoindentation, the evolution of shear bands, including initiation, formation and propagation, was investigated in detail. During a nanoindentation, the shear deformations in the samples were found mainly undergoing three stages, which can be categorized as shear transformation zone initialization, shear band formation and shear band propagation. Shear transformation zones are small regions that local atomic rearrangement occurs without significantly affecting the relative positions of atoms in the immediate vicinity. Shear bands usually evolve from shear transformation zones when local shear stress dominates in one direction. However, not all shear transformation zones can finally turn into shear bands.

The shear transformation zones and shear bands were characterized by the local deviatoric shear strains as shown in Fig. 2. In the bulk sample, N-Bulk, the shear transformation zone nucleates in the region beneath the indenter when the indentation depth is between 1.0 nm and 1.2 nm. The first shear band is formed by extending the shear transformation zone in the direction of 45° away from y-axis. With the increase of the indentation depth, more

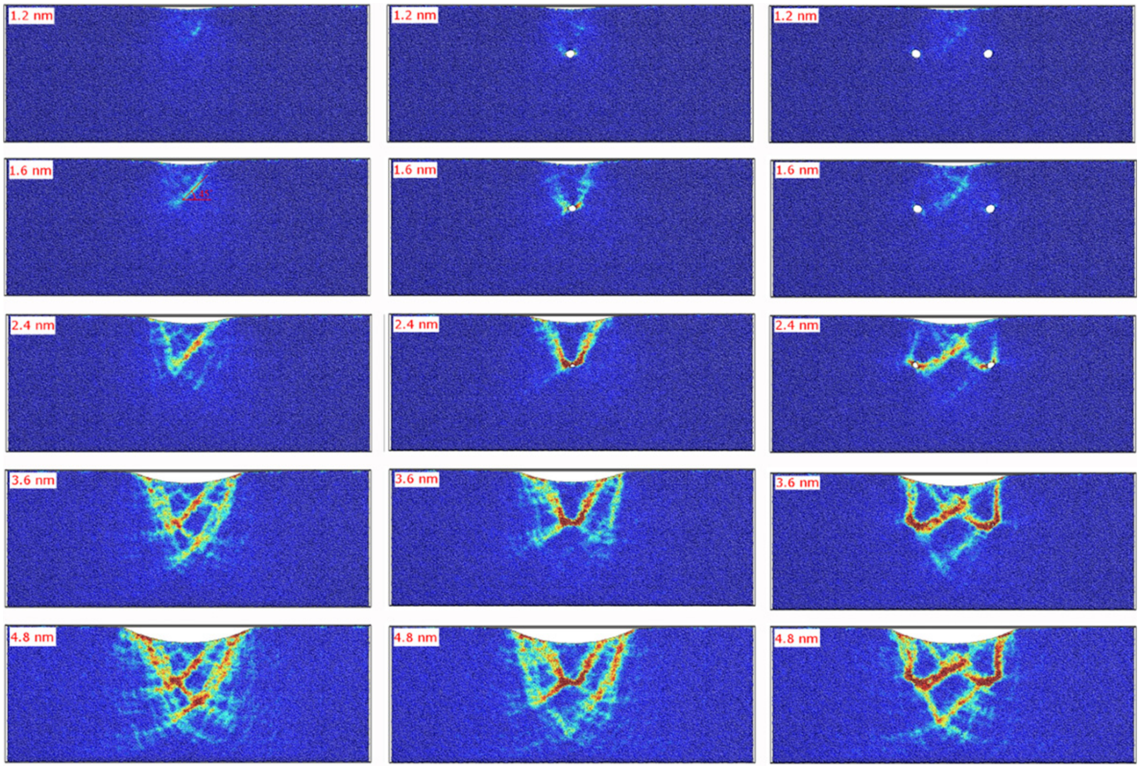

(N-Bulk) (N-A) (N-B)

Fig. 2. Visualizations of local deviatoric shear strains at a series of indentation test steps with a depth varying from 1.2 nm, 1.6 nm, 2.4 nm and 3.6 nm to 4.8 nm. Red represents local deviatoric shear strains saturated at 0.5 while blue denotes local deviatoric shear strains equal or lower than 0.05. (For interpretation of the references to color in this figure legend, the reader is referred to the web version of this article.)

shear bands form and propagate. At an indentation depth of 4.8 nm, the indentation region is fully developed containing a few cross-linked shear bands which accommodate the majority of the shear deformation. The intersections of the shear bands show the highest level of local deviatoric shear strains. The thickness of each shear band is roughly between 2 nm and 4 nm. In addition to major shear bands, many dispersed shear transformation zones exist in the indentation region. Some of these transformation zones are potentially leading to the formation of new shear bands if higher indentation depth applies. Furthermore, substrate provides a strong confinement to the shear deformation. Hence, the shear bands close to the substrate are prone to divert to circumvent the substrate. In contrast, free surface provides no constraints on the propagation of shear bands, which make itself the preferred site where shear bands propagate toward.

According to Hertzian analysis, the maximum shear stress appears on the axis at a finite distance beneath cylindrical indenter for isotropic materials [35,36]. However, the first shear transformation zone in the bulk sample is about 5 nm beneath the indenter, but not along the axis of indentation. Hence, it suggests that the formation of shear transformation zones is not uniquely determined by the maximum local shear stresses. Although metallic glasses are regarded as homogeneous at macroscale, they have vast variations in local configurations at atomic-scale. Each local atomic configuration is associated with different shear resistances, and shear transformation zones usually nucleate at the sites with low shear resistance. Therefore, the variation in local atomic configuration is affecting the positions where shear transformation zones form. Furthermore, the distribution of shear bands is asymmetric although the cylindrical indenter is axisymmetric, which suggests the local atomic configurations change not only the positions of initiation but also the propagation directions of shear bands.

The formation and propagation of shear bands is greatly affected by the pores existing in indentation region. In sample N-A, a single pore is located in the right front of the indenter and the vicinity of the pore becomes the high concentration region of shear strains. Shear transformation zones form at the wings of that single pore, which differ from initiation location in the bulk sample N-Bulk. In sample N-B, two pores are located in the front of indenter, but both out of shear deformation region when indentation depth is small. Hence, the initiation of the shear transformation zones is not much affected by these two pores, and is similar to that observed in the bulk sample N-Bulk. However, the propagation of the shear bands is greatly influenced by those two pores when indentation depth increases. After the shear transformation zone forms, shear bands propagate from the shear transformation zone toward the pores. With further increased indentation depth, more shear bands form and propagate from pores toward the curved contact surface in both samples N-A and N-B.

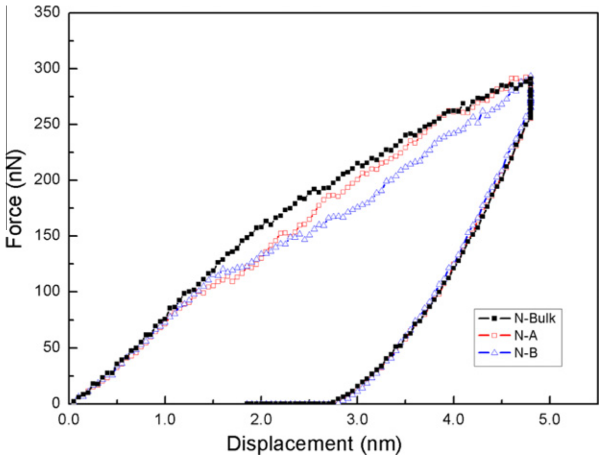

Fig. 3. Force–displacement curves during nanoindentations of samples N-Bulk, N-A and N-B.

The force–displacement curves which represent the *y*-component of interaction forces between indenter and samples during nanoindentations are shown in Fig. 3. Three samples have almost the same force–displacement curves at the starting of the nanoindentations. At that stage, all samples have no shear transformation zones formed yet and they deform elastically. Three force–displacement curves start to diverge at indentation depth from 1.0 nm to 1.2 nm which is the period when shear transformation zones form according to the visualization results discussed above. The reason of this divergence is that the pores weaken the strength of material within the indentation region by affecting the shear transformation zones. After the indentation depth reaches 1.75 nm, shear softening happens accompanying the formation of shear bands and it corresponds to the step-wise curves in Fig. 3.

When pores are involved into the propagation paths of the shear bands, the strength of metallic glasses is reduced. Sample N-A has a lower strength than bulk sample N-Bulk but a higher one than sample N-B. Therefore, it is suggesting that the more pores interacting with shear bands, the greater the reduction in strength of porous metallic glasses. In addition, two pores can accommodate more shear deformation than one pore, and the annihilation of pores in sample N-B is postponed compared to that in sample N-A. After the pores have collapsed, the strengths of the porous samples converge to that of the bulk sample. All the samples creep during the holding period at the maximum indentation depth and then follow almost the same curves in unloading. Basically the data from the strength of the bulk sample N-Bulk offers an envelope in the force–displacement curves.

The equivalent hardness is extracted from the force–displacement curves, following the definition of hardness,

$$H = \frac{P}{A_c} \tag{4}$$

in which, P is the loading force, and A_c is the projected contact area, while H is the hardness. All these quantities are statistically calculated in a short period at the end of loading. At the indentation depth of 4.8 nm, all bulk and porous samples have a close hardness value and shows no effect relating to porosity. It suggests that the hardness of porous samples converges to the value of bulk sample after pores collapsed. The maximum loading force is evaluated at 296 ± 10 nN for all samples. According to the ideal contact profile, the projected contact area would be 95.0 nm^2 at 4.8 nm indentation depth. However, a small amount of sink-in happens during nanoindentation of all three samples. Alternatively, the projected contact area is directly evaluated by examining the profile of indentation compression, which is 85.5 ± 0.5 nm^2 for all three samples. According to Eq. (4), the equivalent hardness is calculated as 3.46 ± 0.15 GPa, which is lower than the Vickers hardness of common Cu/Zr-based metallic glasses ($\sim$5 Gpa), and it is possibly caused by different nanoindenter profiles [37]. It indicates that the current model can capture the behaviours of shear bands and pores, but for a more quantitative analysis, a more accurately calibrated model is required.

3.2. Mechanical behaviours of metallic glasses under uniaxial compression

In the MD simulations of uniaxial compression, the mechanical behaviours of metallic glasses are determined as well as the evolution of shear bands. Shear transformation zones and shear bands are still characterized with local deviatoric shear strains at several critical stages as shown in Fig. 4. Except for using local deviatoric shear strains, the global compressive strain is also used to represent the magnitude of deformation in the entire sample, which is simply the y-component of true compressive strain.

In the bulk sample C-Bulk, shear transformation zones are initiated when the global compressive strain is between 5% and 6%. After this, the shear transformation zones extend along a direction 45° away from compression direction. The distribution of shear transformation zones in the bulk sample C-Bulk shows concentration on a series of parallel lines with a spacing of 8–10 nm. As the global compressive strains increasing, shear transformation zones link together and merge into large shear bands with an orientation of around 45° away from the loading direction. The major shear bands widen because more adjacent atoms are involved in the evolution of the shear bands. It is observed that the shear deformation is highly localized in major shear bands. The local deviatoric shear strains in other regions are relatively small compared to that in major shear bands.

In both nanoindentation and uniaxial compression, the initiation of first shear bands aligns along the direction with an angle of 45° away from loading axis, which is coincident with the maximum shear stress direction of isotropic materials [35]. However, the location that shear bands initialize differs in two loading conditions. In nanoindentation, the curved indenter surface introduces deviatoric stresses along contact interfaces, and all major shear

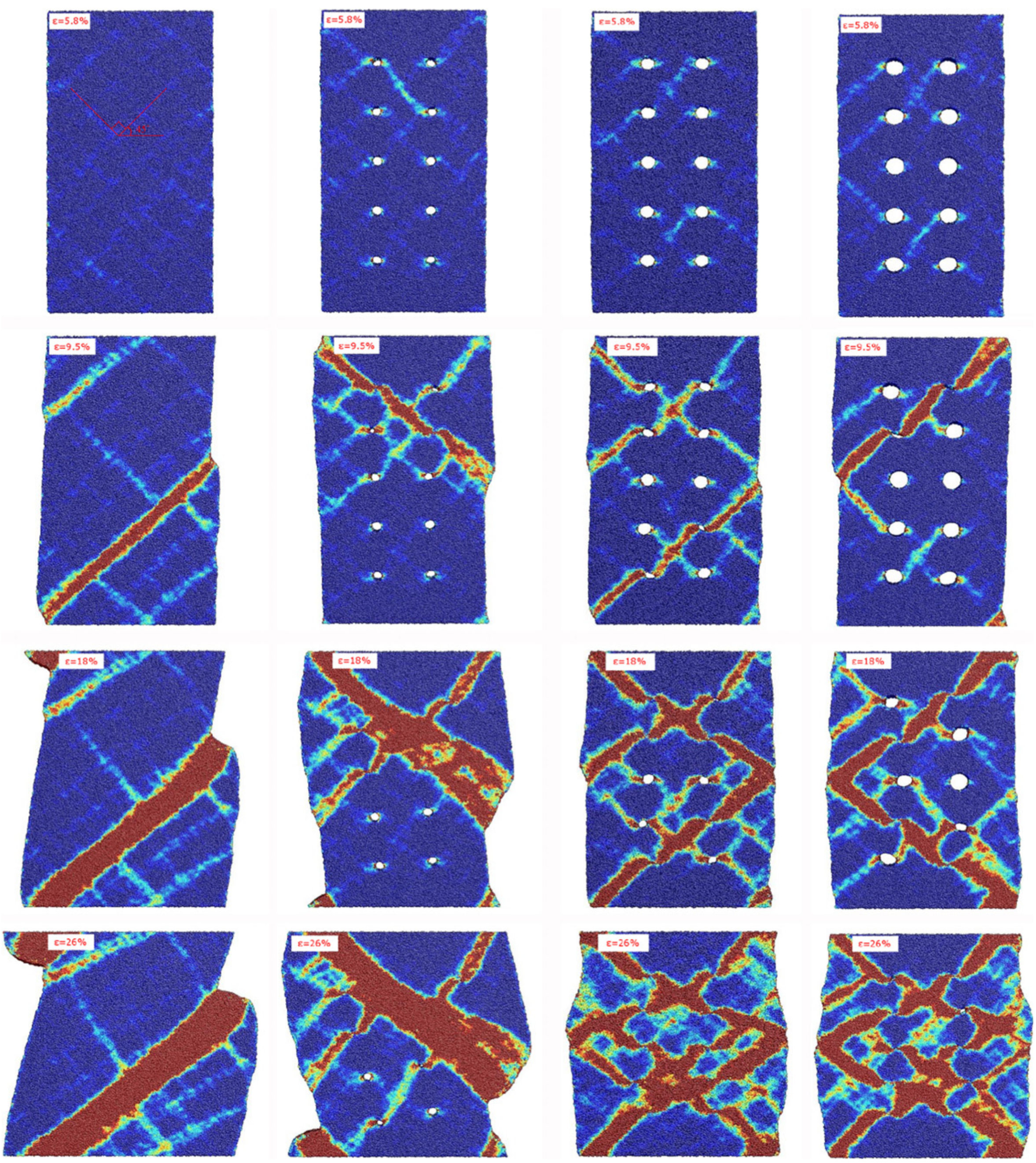

(C-Bulk) (C-PI) (C-PII) (C-PIII)

Fig. 4. Visualization of local deviatoric shear strains at 5.8%, 9.5%, 18%, and 26% global compressive strains in the samples C-Bulk, C-PI, C-PII and C-PIII. Red represents local deviatoric shear strains saturated at 0.5, while blue denotes local deviatoric shear strains equal or lower than 0.05. (For interpretation of the references to color in this figure legend, the reader is referred to the web version of this article.)

bands initiate or end at contact interfaces. In contrast, deviatoric stresses are only caused by the Poisson's effect in uniaxial compression. Hence, the free surface is the preferred site to initiate shear bands in uniaxial compression. Furthermore, the propagation of shear bands also varies in two different loading conditions. Shear bands are confined in the indentation region during nanoindentation, but they propagate across the whole sample in uniaxial compression. Hence, an radial shear banding pattern exhibits in nanoindentation, while a parallel shear banding pattern shows in uniaxial compression.

In porous samples, the behaviours of shear bands are greatly affected by the existence of pores. Shear transformation zones form in the vicinity of pores with 4–5% global compressive strains, which is slightly earlier than in the bulk sample. It is corroborated that pores greatly facilitate the formation of shear bands according to the results obtained from nanoindentations. Within 5.8% global compressive strains, shear bands have formed in all porous samples. Shear bands propagate either along the line connecting two diagonal pores or from one pore to the free edges of samples. The orientations of shear bands are still along the direction 45° away from the compression direction in these porous samples. As deformation increases, pores on the propagation path of major shear bands collapse and it increases the shear resistance of major shear bands. When a major shear band stops due to the high shear resistance on its path, new shear bands form along low shear resistance path to allow further shear deformation.

During uniaxial compressions, the size effect of pores is also found on the initiation and propagation of shear bands in porous metallic glasses. In the porous sample C-PI, the major shear band is still active after interior pores have collapsed, and it continues to engage more atoms and pores nearby to dissipate the shear deformation. Small shear bands arise from the major shear bands and propagate along directions perpendicular to major shear bands, accommodating shear deformation at the mean time. In the porous samples C-PII and C-PIII, the major shear bands stop propagating after the interior pores have collapsed and then new shear bands take over the role of carrying the shear deformation, and the orientation of the new shear band is conjugate to that of the died major shear band.

At 26% strain, both the bulk sample C-Bulk and the porous sample C-PI show highly localized shear deformation along major shear bands while the porous samples C-PII and C-PIII have evenly dispersed deformation areas as a consequence of formation of multiple major shear bands. In addition, several pores are retained at 26% global compressive strain in the porous sample C-PI while all pores have collapsed in porous samples C-PII and C-PIII. As a result, the bulk sample C-Bulk and the porous sample C-PI are more likely to have a catastrophic failure than porous samples C-PII and C-PIII.

The material properties of samples at the microscale can be further determined by extracting stress–strain curves of the uniaxial compressions. The normal pressures on the top and bottom boundaries of *y* dimension are outputted as uniaxially-compressive stresses, which is actually the *y*-component of true stress of uniaxial compression. The stress–strain curves of the uniaxial compressions of all samples are shown in Fig. 5. In general, shear softening occurs in all samples, which contribute to the formation of shear bands. The shear resistance also evolves, corresponding to the annihilation of pores and the stopping of shear bands during deformation. After the global compressive strains reaches 14%, porous sample C-PII and C-PIII have higher shear resistances than bulk sample C-Bulk and porous sample C-PI. The effect of pores on facilitating the initiation of shear bands is also indicated by the stress–strain curves in Fig. 5. It shows that the shear softening of these metallic glasses happen at around 5.8% global compressive strains, which is consistent with the initiation of major shear bands observed in Fig. 4. It also shows that pores reduce the strength of materials in two aspects: (i) the porous materials yield at a lower strain level than the bulk metallic glasses and (ii) the porous materials with larger pores yield earlier than those with smaller pores.

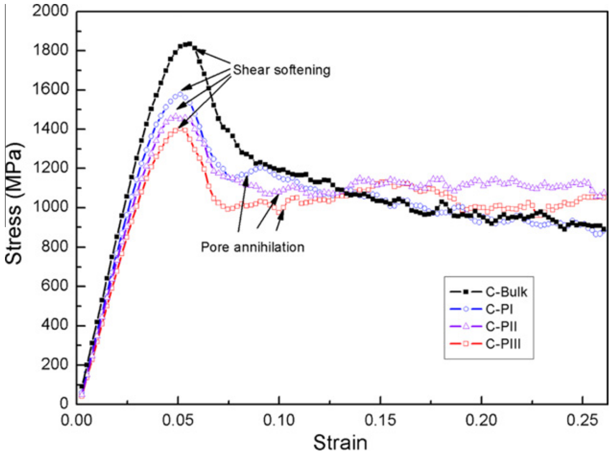

Fig. 5. Stress–strain curves of samples C-Bulk, C-PI, C-PII and C-PIII under unaxial compression.

The elastic modulus is calculated from the linear portion of the stress–strain curve, and the strength before shear softening is taken as the yield strength, which are listed in Table 2. It shows that elastic modulus and yield strength of porous metallic glasses decrease as the porosity increases, which has also been found in experimental results [20,22]. It is noticed that the elastic modulus of bulk $Cu_{46}Zr_{54}$ metallic glasses, 44.0 GPa, is higher than the value calculated by Shimizu et al., 38.0 GPa at 300 K [38]. As the uniaxial compressions were performed at 100 K in current model, this difference is attributed to the effect of temperature on the elastic modulus. However, the elastic modulus calculated from current uniaxial compression model is still much lower than the experimental results, which is 82–107 GPa for Cu/Zr-based metallic glasses [37,39].

In addition, beyond the first peak there is evidence of hardening of the porous metallic glasses in the stress–strain curves after the pores have collapsed at larger shear deformations. The explanation for this type of hardening is that the annihilation of the pores increases the shear resistance for the major shear bands by two means. Firstly, the length of the shear band path increases. Secondly, there is a misalignment between shear-band segments after pores have collapsed, because shear bands shifted by a distance that equals the diameter of the pores. However, when a new shear band forms and propagates, another shear softening usually occurs, as the new shear band has lower shear resistance than the existing ones.

Although experimental results have already shown that the existence of pores improves the ductility of metallic glasses [20,22], the role of pores' size should be further clarified. From current simulation results, the pores' size appears to be critical in determining shear banding behaviours and the ductility of porous metallic glasses. Only pores reaching a critical size can dissipate

Table 2
Mechanical properties of bulk and porous samples under uniaxial compression.

	Porosity (%)	Elastic modulus (GPa)	Yield strength (MPa)
C-Bulk	–	44.0	1830
C-PI	2.4	41.0	1578
C-PII	4.3	39.3	1464
C-PIII	6.8	36.6	1404

shear deformation effectively, as shown in sample C-PII and C-PIII, and those under the critical size have less impact on shear bands, as shown in sample C-PI. Porous metallic glasses with larger pores are more likely to form multiple major shear bands, allowing larger plastic deformation before failure, while those with smaller pores behaves similar as bulk metallic glasses. Generally, the porous metallic glasses with smaller pores required higher local strains to initiate shear bands than those with larger pores. Several small pores in C-PI were retained with little change in their shape even at 26% global compressive strains. However, the critical size of pores that turning porous metallic glasses from bulk-like into multiple shear banding mode has not be precisely identified from current simulation results.

Furthermore, the orientations of major shear bands also affect the ultimate shear resistances of these glasses. In porous samples C-PII and C-PIII, the orientations of active major shear bands vary at different stages of uniaxial compression and the samples slip in a pair of conjugated directions rather than slipping in a single direction or several parallel directions. As the slipping directions are conjugated, the shear bands are cross-linked and block one another, resulting in an increase in shear resistance. The shear deformation in the bulk sample C-Bulk and the porous sample C-PI are both dominated by one major shear band, such that are no hardening effect from such blockage of shear bands. Therefore, porous metallic glasses with cross-linked major shear bands have higher ultimate shear resistance than those with a single shear band or several paralleled major shear bands as shown in the stress–strain curves in Fig. 5. Note that the increase in shear resistance is a great contribution to the energy absorption of porous metallic glasses as well.

4. Conclusions

In the work, to capture the evolution of shear bands and determine the material properties of $Cu_{46}Zr_{54}$ metallic glasses, we modelled nanoindentation and uniaxial compression tests on bulk and nano-porous $Cu_{46}Zr_{54}$ metallic glasses by using molecular dynamics (MD) simulations. The shear transformation zones and shear bands were characterized through visualization of the local deviatoric shear strains. The simulation results revealed several important aspects of the deformation mechanism in nano-porous metallic glasses, as follows:

- Pores act as local strain concentrators and reduce the shear resistance of porous metallic glasses. Shear bands usually initiate in the vicinity of pores and propagate out in a direction of around 45° away from a loading direction. The yielding strength and elastic limit are both reduced in porous metallic glasses, due to softening effects caused by pores.
- The size of the pores greatly influences the initiation and propagation of shear bands in the metallic glasses. Larger pores are more effective in reducing the shear resistance than smaller ones. Porous metallic glasses with smaller pores behave similarly to bulk metallic glasses but form small shear bands stemming from major shear bands. In contrast, those with large pores have multiple major shear bands developing at different stages and possess higher ultimate shear resistances.
- Under large compressive deformations, porous metallic glasses exhibit hardening effects when a pore collapses or a shear band stops. Due to the blockage of shear bands, cross-linked shear bands are more valuable in improving the ductility and energy absorption than a single shear band or parallel major shear bands.

Acknowledgements

P.D. Hodgson and C. Yang would like to acknowledge the financial support from the ARC Centre of Excellence for the Design of Light Metals and the Australian Laureate Fellowshipfor P.D. Hodgson. The authors are grateful to the Victorian Partnership for Advanced Computing (VPAC), Australia for its high performance computing resources.

References

[1] W.L. Johnson, JOM Journal of the Minerals, Metals and Materials Society 54 (2002) 40–43.
[2] A. Inoue, A. Takeuchi, Materials Science & Engineering A 375 (2004) 16–30.
[3] W.H. Wang, C. Dong, C.H. Shek, Materials Science and Engineering R 44 (2004) 45–89.
[4] C. Schuh, T. Hufnagel, U. Ramamurty, Acta Materialia 55 (2007) 4067–4109.
[5] A. Yavari, J. Lewandowski, J. Eckert, MRS Bulletin 32 (2007) 635–638.
[6] W. Johnson, MRS Bulletin 24 (1999) 42–56.
[7] D.C. Hofmann, J.-Y. Suh, A. Wiest, G. Duan, M.-L. Lind, M.D. Demetriou, W.L. Johnson, Nature 451 (2008) 1085–1089.
[8] R.D. Conner, W.L. Johnson, N.E. Paton, W.D. Nix, Journal of Applied Physics 94 (2003) 904.
[9] C.C. Hays, C.P. Kim, W.L. Johnson, Physical Review Letters 84 (2000) 2901–2904.
[10] T.C. Hufnagel, P. El-Deiry, R.P. Vinci, Scripta Materialia 43 (2000) 1071–1075.
[11] Y. Shi, M.L. Falk, Acta Materialia 55 (2007) 4317–4324.
[12] S. Ogata, F. Shimizu, J. Li, M. Wakeda, Y. Shibutani, Intermetallics 14 (2006) 1033–1037.
[13] F. Shimizu, S. Ogata, J. Li, Materials Transactions 48 (2007) 2923.
[14] B. Yang, M.L. Morrison, P.K. Liaw, R.A. Buchanan, G. Wang, C.T. Liu, M. Denda, Applied Physics Letters 86 (2005) 141904.
[15] B. Yang, T.G. Nieh, Acta Materialia 55 (2007) 295–300.
[16] Y. Shi, M.L. Falk, Acta Materialia 56 (2008) 995–1000.
[17] A.H. Brothers, D.C. Dunand, Scripta Materialia 54 (2006) 513–520.
[18] J. Jayaraj, B.J. Park, D.H. Kim, W.T. Kim, E. Fleury, Scripta Materialia 55 (2006) 1063–1066.
[19] J. Jayaraj, J.M. Park, P.F. Gostin, E. Fleury, A. Gebert, L. Schultz, Intermetallics 17 (2009) 1120–1123.
[20] T. Wada, A. Inoue, A.L. Greer, Applied Physics Letters 86 (2005) 251907.
[21] T. Wada, M. Kinaka, A. Inoue, Journal of Materials Research 21 (2006) 1041–1047.
[22] A. Inoue, T. Wada, D. Louzguine-Luzgin, Materials Science & Engineering A 471 (2007) 144–150.
[23] A. Brothers, D. Dunand, MRS Bulletin 32 (2007) 639–643.
[24] V. Rosato, M. Guillope, B. Legrand, Philosophical Magazine A 59 (1989) 321–336.
[25] F. Cleri, V. Rosato, Physical Review B 48 (1993) 22–33.
[26] G. Duan, D. Xu, Q. Zhang, G. Zhang, T. Cagin, W.L. Johnson, W.A. Goddard Iii, Physical Review B 71 (2005) 224208.
[27] J. Wang, P. Hodgson, J. Zhang, W. Yan, C. Yang, Journal of Materials Processing Technology 209 (2009) 4601–4606.
[28] W.G. Hoover, Physical Review A 31 (1985) 1695–1697.
[29] H.C. Andersen, The Journal of Chemical Physics 72 (1980) 2384.
[30] W.G. Hoover, Physical Review A 34 (1986) 2499–2500.
[31] S. Melchionna, G. Ciccotti, B.L. Holian, Molecular Physics 78 (1993) 533–544.
[32] S. Plimpton, Journal of Computational Physics 117 (1995) 1–19.
[33] J. Li, Modelling and Simulation in Materials Science and Engineering 11 (2003) 173–177.
[34] M.L. Falk, Physical Review B 60 (1999) 7062–7070.
[35] K. Johnson, Contact Mechanics, Cambridge University Press, 1987.
[36] C.E. Packard, C.A. Schuh, Acta Materialia 55 (2007) 5348–5358.
[37] W.H. Wang, Journal of Non-Crystalline Solids 351 (2005) 1481–1485.
[38] F. Shimizu, S. Ogata, J. Li, Acta Materialia 54 (2006) 4293–4298.
[39] D. Xu, B. Lohwongwatana, G. Duan, W.L. Johnson, C. Garland, Acta Materialia 52 (2004) 2621–2624.